RSC Advances

ROYAL SOCIETY OF CHEMISTRY

www.rsc.org/advances

Cite this: DOI: 10.1039/c0xx00000x

www.rsc.org/xxxxxx

ARTICLE TYPE

Rapid microwave-assisted fabrication of 3D cauliflower-like $NiCo_2S_4$ architectures for asymmetric supercapacitors

Yanling Xiao,[a] Ying Lei,[b] Baozhan Zheng,[a] Li Gu,[a] Yanyan Wang[b] and Dan Xiao*[ab]

Received (in XXX, XXX) Xth XXXXXXXXX 20XX, Accepted Xth XXXXXXXXX 20XX

DOI: 10.1039/b000000x

In this study, 3D cauliflower-like $NiCo_2S_4$ architectures have been synthesized through a facile, one-step and without any template microwave method. The cauliflower-like $NiCo_2S_4$ materials are made up of 3D microstructures with an average diameter of around 600 nm and each nanostructure is found to be constructed by many intertwined nanoparticles. The $NiCo_2S_4$-modified electrode has been successfully applied to pseudocapacitor. The electrochemical performance of the $NiCo_2S_4$ was studied by cyclic voltammetry, galvanostatic charge-discharge and electrical impedance spectroscopy. The 3D cauliflower-like $NiCo_2S_4$ materials exhibit a maximum capacitance of 1471 F g^{-1} at 1 A g^{-1} and also show remarkable rate capability and prominent cycle stability. To improve the energy density of supercapacitor, the $NiCo_2S_4$-modified electrode and activated carbon-modified electrode were used to assemble an asymmetric capacitor. The asymmetric capacitor demonstrates remarkable properties with a maximum energy density of 44.8 Wh kg^{-1} and a maximum power density of 16.0 kW kg^{-1}. Furthermore, two capacitors assembled together can successfully light up a red light-emitting diode (LED) and last for more than 10 min. The excellent capacitance performance demonstrates that the cauliflower-like $NiCo_2S_4$ has potential applications in supercapacitors.

Introduction

In order to address rapidly increasing energy crisis, much efforts have been devoted to exploring and designing new sustainable and environmental friendly products by scientists for decades.[1,2] Electrochemical capacitors (ECs), as promising candidates for power sources storage devices, which fill the gaps between batteries and traditional electrostatic capacitors, have attracted much attention due to their higher power and energy densities, fast charging, long cycle life.[3-5] The electrode materials of the ECs usually consist of conducting polymers, transition metal oxides/hydroxides and carbon materials. However, carbon materials and conducting polymers usually have low specific capacitance and poor cycling stability, respectively. The poor electrochemical property of these materials impedes their practical applications.[6,7] Interestingly, transition metal oxides/hydroxides usually have a variety of oxidation states which facilitate faradaic reactions, achieving much more prominent specific capacitance.[8,9]

Among transition metal oxides materials, binary metal oxide, such as $NiCo_2O_4$, is a potential material for supercapacitor. It is reported that $NiCo_2O_4$ is endowed with higher conductive ability, at least ~100 times higher than Co_3O_4 and NiO, which enables it to be a outstanding electrode material.[10,11] Similar to $NiCo_2O_4$, nickel cobalt sulphide ($NiCo_2S_4$) materials are also applied to supercapacitors and other applications.[12-15] $NiCo_2S_4$ possesses richer redox ability than the single phase of metal sulfides due to its synergistic effect from both nickel and cobalt ions.[16] Furthermore, $NiCo_2S_4$ shows much higher conductivity compared to $NiCo_2O_4$.[17] Up to now, many methods for synthesizing $NiCo_2S_4$ electrode materials have been reported, such as hydrothermal method and electrodeposition.[10,17-20] For example, Xia *et al*. have synthesized 3D urchin-like $NiCo_2S_4$ using a multistep hydrothermal method without any templates.[17] Furthermore, Ruan and co-workers have fabricated porous $NiCo_2S_4$ nanotubes via hydrothermal method and sacrificial templates.[19] In addition, Alshareef *et al.* have proposed $NiCo_2S_4$ nanosheet arrays by electrodeposition.[20] Although the electrode materials fabricated by the two strategies usually have relatively high specific capacitances, their some disadvantages still greatly hinder their practical applications. The hydrothermal method generally involves multistep procedure and even need some templates, which make the preparation of the electroactive materials complicated and time-consuming. What's more, hydrothermal reaction has relatively rigorous requirements for safety and quality of the equipments due to the generated relatively high temperature and high pressure during hydrothermal reaction, which will increase the cost undoubtedly. For electrodeposition, it needs a long time to deposit one electrode and use the expensive equipment (electrochemical workstation). Therefore, the electrodeposition is also costly and

time-consuming. By contrast, microwave-assisted heating (MWH) method involves simple and easy operation, greatly shortening the reaction time and easily forming a uniform reaction system. Moreover, most materials can be prepared by a simple one-step microwave-assisted method just by employing a household microwave oven without any templates. In a word, the MWH is a facile, low-cost, template-free, one-step method, and can be used for large-scale application. Therefore, MWH can be applied to the preparation of different inorganic materials.[21, 22]

In this paper, we present a facile MWH method to prepare 3D cauliflower-like $NiCo_2S_4$. The cauliflower-like $NiCo_2S_4$ acting as supercapacitor electrode material displays high specific capacitance, remarkable rate performance and prominent cycle properties. To further study the practical application of $NiCo_2S_4$, an asymmetric capacitor was assembled. Fortunately, the as-fabricated asymmetric supercapacitor exhibits high energy and power densities, which is able to drive a low voltage device such as LED.

Experimental section

Synthesis of 3D cauliflower-like $NiCo_2S_4$ architectures

All the analytical grade chemicals were used directly. In this typical experiment, 5 mmol of $Ni(NO_3)_2$•$6H_2O$, 10 mmol of $Co(NO_3)_2$•$6H_2O$, 10 mmol of citric acid (H_3Cit) and 30 mmol of thioacetamide (CH_3CSNH_2) were dissolved in 100 mL of ethylene glycol (EG) solution with magnetic stirring. Then, the mixture was treated for 5 min at 700 W in the household microwave oven. After that, the products were obtained by centrifugal filtration and rinsed with deionized water and absolute ethanol, respectively. The final products were dried at 50 ^oC overnight under vacuum conditions.

Characterization

The composition and crystal structure of $NiCo_2S_4$ materials were investigated by X-ray powder diffractometer (XRD, Tongda TD-3500, Liaoning, China, Cu-Kα radiation, λ = 0.15148 nm) operated at 30.0 kV and 20.0 mA. The morphology and structure of $NiCo_2S_4$ materials were conducted using a scanning electron microscope (SEM, Hitachi S4800, Tokyo, Japan) attached with energy dispersive spectra (EDS) and a transmission electron microscopy (TEM), high resolution transmission electron microscopy (HRTEM, Hitachi H-800, operated at 200.0 kV). The X-ray photoelectron spectra (XPS, Kratos XSAM 800, Manchester, U.K., Mg-Ka, 1253.6 eV) were acquired to investigate the composition on the near-surface of $NiCo_2S_4$ materials. The Brunauer-Emmett-Teller (BET) surface area and pore size distribution of the $NiCo_2S_4$ materials were conducted from N_2 adsorption-desorption at 77.3 K through a Automated Surface Area and Pore Size Analyzer (Quadrasorb SI).

Electrochemical characterization

The electrochemical performance of resultant $NiCo_2S_4$ material was measured in a traditional three-electrode system, where $NiCo_2S_4$-modified electrode, a graphite sheet and a Hg/HgO electrode act as the working, counter and reference electrodes, respectively. And the working electrodes were fabricated as follows. 80 wt % of $NiCo_2S_4$ material (electroactive material), 15 wt % of acetylene black (conducting material) and 5 wt % of poly (vinylidene fluoride, PVDF, binder) were mixed and dissolved in a certain amount of N-Methyl-2-pyrrolidne (NMP, solvent). Then, the mixture was loaded onto the nickel foam substrate (surface, 1.0 cm × 1.0 cm). The as-prepared $NiCo_2S_4$-modified electrodes were dried at 60 ^oC for 12 h under vacuum. After that, the $NiCo_2S_4$-modified electrodes were pressed under a pressure of 10 MPa. The mass loading of $NiCo_2S_4$ electroactive materials was about 3.5-5.0 mg.

In half-cell tests, all electrochemical experiments of the $NiCo_2S_4$-modified electrode were conducted by an Autolab PGSTAT 30/302 electrochemical workstation (Eco Chemie B.V., Amsterdam, the Netherlands). Cyclic voltammetry (CV), galvanostatic charge-discharge and electrical impedance spectroscopy (EIS) were carried out to investigate the electrochemical properties of the obtained $NiCo_2S_4$-modified electrodes. EIS tests of the as-synthesized $NiCo_2S_4$-modified electrodes were performed with a frequency loop 10 kHz-10 mHz under open circuit voltage with an ac amplitude of 10 mV. The electrodes are first activated for a while until the specific capacitance basically doesn't increase.

For full cell tests, the asymmetric capacitors were fabricated to evaluate the $NiCo_2S_4$ electrode for practical application. The electrochemical performance was conducted in two-electrode system. The $NiCo_2S_4$ electrodes were acted as the positive electrode and the activated carbon (the synthetic details and the BET surface area details in Fig. S7, ESI) electrodes served as the negative electrode. The two asymmetric supercapacitors could power a LED indicator.

Results and discussion

Structure and morphology of 3D cauliflower-like $NiCo_2S_4$ architectures

To investigate the crystallinity and phase purities of the product, we resorted to XRD measurement and the corresponding result is demonstrated in Fig. 1. As depicted in Fig. 1, the distinctive peaks at 26.8 °, 31.5 °, 38.1 °, 50.4 ° and 55.2 °can be observed and they accord with (220), (311), (400), (511) and (440) planes, respectively. All the reflection peaks of the as-prepared products can be well indexed to the $NiCo_2S_4$ (JCPDS card No. 20-0782) according to the previous reports.[13,14,19] The diffraction peaks can be assigned to cubic type $NiCo_2S_4$. Near absence of impurity peaks appeared in the XRD pattern indicates that high purity $NiCo_2S_4$ is obtained through our proposed synthesis method.

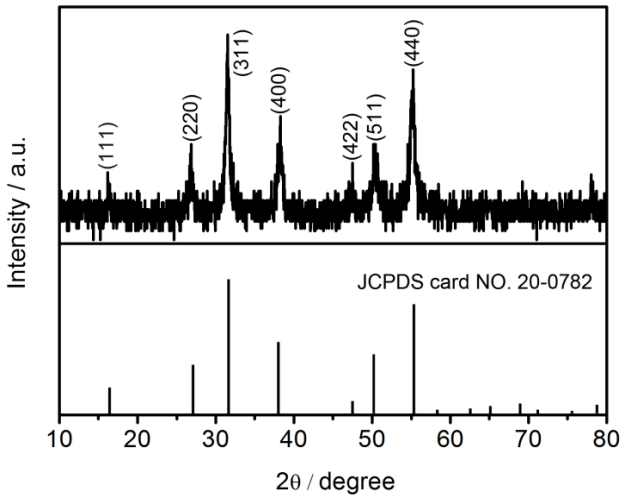

Fig. 1 Typical XRD pattern of the 3D cauliflower-like $NiCo_2S_4$ architectures.

To further understand the composition of the $NiCo_2S_4$ samples, the EDS and XPS tests were carried out and the corresponding results are demonstrated in Fig. 2. Only the peaks of Ni, Co, S elements appear in the EDS spectrum (Fig. 2a), which suggests that the $NiCo_2S_4$ material is mainly composed of Ni, Co, S elements. Fig. 2b-d present the XPS spectra of Ni, Co and S. As shown in Fig. 2b, two strong peaks in the Co 2p spectrum at 778.7 eV and 793.9 eV are observed and can be assigned to Co $2p_{3/2}$ and Co $2p_{1/2}$.[12,23] The Co $2p_{3/2}$ and Co $2p_{1/2}$ with a spin-energy separation of 15.2 eV demonstrates the coexistence of Co^{2+} and Co^{3+}.[23] From the Ni 2p spectrum (Fig. 2c), we can clearly observe two kinds of Ni species (Ni^{2+} and Ni^{3+}). The fitting peaks at 853.2 and 871.0 eV are assigned to Ni^{2+}, and another two peaks at 854.9 and 872.6 eV are ascribed to Ni^{3+}.[24,25] In addition, the relative content of Co^{2+} and Co^{3+} as well as Ni^{2+} and Ni^{3+} in the $NiCo_2S_4$ materials is presented in the Table S1 in the electronic supplementary information. The amount of Co^{2+}, Co^{3+}, Ni^{2+} and Ni^{3+} are 32.00, 68.00, 64.90, and 35.1%, respectively. The peak at 163.4 eV is a typical of metal-sulphur bond.[17,18] Obviously, the XPS data demonstrate that the near-surface of the $NiCo_2S_4$ materials have a composition containing S^{2-}, Ni^{3+}, Ni^{2+}, Co^{3+}, Co^{2+}, which is consistent with the conclusions in the reported literatures for $NiCo_2S_4$.[17]

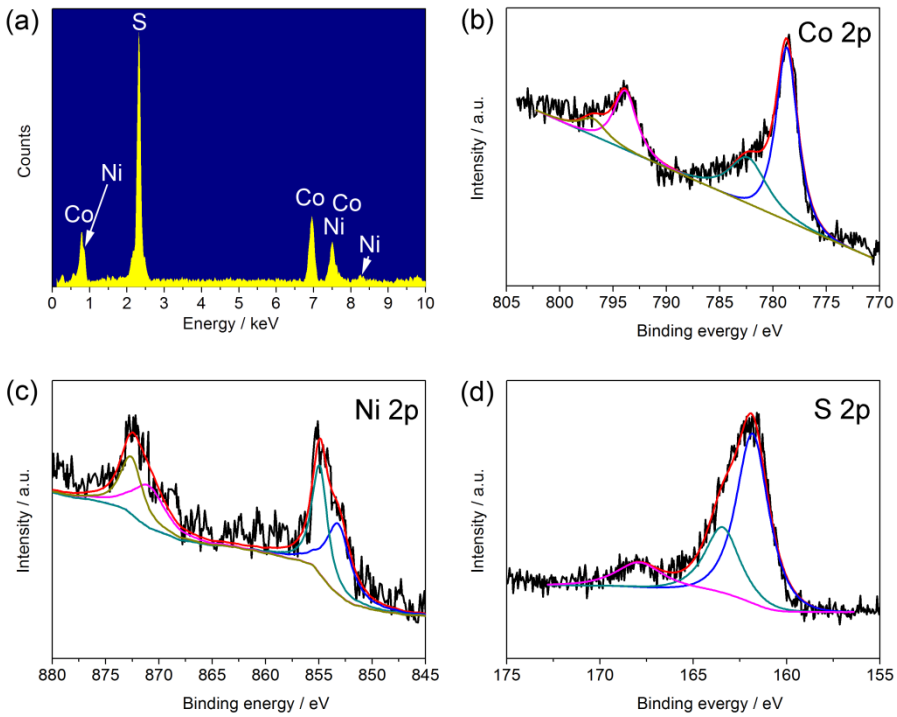

Fig. 2 (a) EDS image, (b) Ni 2p, (c) Co 2p, and (d) S 2p XPS spectra of the 3D cauliflower-like $NiCo_2S_4$ architectures.

The morphology and the crystalline structure of the obtained $NiCo_2S_4$ materials were demonstrated by the SEM, TEM and HRTEM. Fig. 3a presents a representative SEM image of the $NiCo_2S_4$ materials. Apparently, the SEM image presents that the $NiCo_2S_4$ is made up of 3D microstructures with an average diameter of approximately 600 nm. Furthermore, it is found that each nanostructure is made up of numerous $NiCo_2S_4$ nanoparticles. Fig. 3b is the picture of cauliflower. Comparing the Fig. 3a and b, it can be observed that the shape of the $NiCo_2S_4$ materials is extremely similar to that of cauliflower. As is depicted in Fig. 3c, we can clearly see that the 3D cauliflower-like $NiCo_2S_4$ samples attach to each other and form some nanoclusters. The TEM images in Fig. 3d and e display that there are some obvious small protuberances on the surface of cauliflower-like $NiCo_2S_4$ samples. Apparently, it is also found that the cauliflower-like architectures are inclined to aggregate in groups according to the TEM images, which is in agreement with the images of SEM. The HRTEM image (Fig. 3f) presents that the lattice phase grows along with random orientation. The

interlayer spacings between adjacent lattice stripes are calculated to be around 0.285 and 0.235 nm, which can respectively be ascribed to the (311) and (400) planes of the cubic $NiCo_2S_4$, indicating the polycrystalline characteristic of the 3D cauliflower-like $NiCo_2S_4$ architectures. The result is consistent with other literatures.[13,17] The as-synthesized cauliflower-like $NiCo_2S_4$ with polycrystalline structures are expected to deliver outstanding electrochemical characteristics.

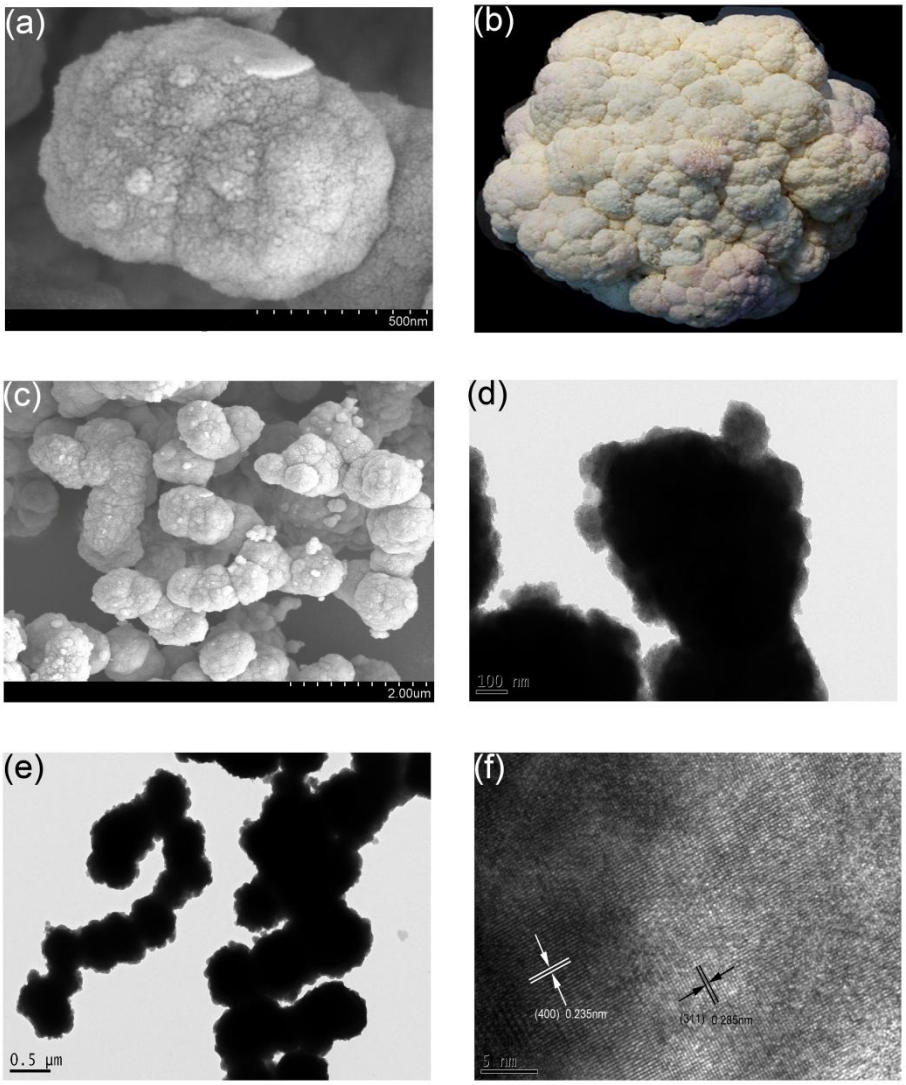

Fig. 3 (a and c) SEM images, (b) the picture of cauliflower, (d and e) TEM images, (f) HRTEM image of the 3D cauliflower-like $NiCo_2S_4$ architectures.

Growth mechanism of 3D cauliflower-like $NiCo_2S_4$ architectures

In order to present the growth mechanism of the 3D cauliflower-like $NiCo_2S_4$ architectures clearly, a series of experiments were performed in different stages of reaction. The corresponding SEM images of the materials obtained at various reaction stages are shown in Fig. 4. As shown in Fig. 4a, the species consisting of numerous nanoparticles was obtained after a very short time (1.5 min). As the reaction time continues to 3 min, some solid microspheres (Fig. 4b) are formed from the cluster of the nanoparticles. After 5 min, the typical cauliflower-like $NiCo_2S_4$ architectures (Fig. 4c) are formed gradually. These SEM images suggest that the shape and size of the materials change gradually along with the reaction time. The XRD patterns of the samples collected at different reaction time were also conducted and the corresponding results are shown in Fig. S1. As shown in the black curve in Fig. S1, there is no obvious diffraction peaks presented in the XRD pattern of the samples collected at the early stage of the reaction (1.5 min). As the reaction continues (3 min), the diffraction peaks of $NiCo_2S_4$ with some impurity peaks in the XRD pattern are presented (Fig. S1, red curve). At a reaction time of 5 min, all of the diffraction peaks are well indexed to the $NiCo_2S_4$. These results suggest that the formation of the $NiCo_2S_4$ crystal could be manipulated by orientation growth kinetics.[26]

Based on the results obtained above, the formation mechanism of the cauliflower-like $NiCo_2S_4$ architectures is tentatively presented. Also, the plausible growth process is depicted in Fig. 5. As is well-known, the functional group –COOH of the H_3Cit in a homogenous system, could be inclined to react with Co^{2+} and

Ni^{2+} to form stable complexes.[27] At the early stage of the reaction, the sulfur atoms of the thioacetamide are replaced by the oxygen atoms from H_2O and produce H_2S. The H_2S could react with the complexes to produce the initial $NiCo_2S_4$ seeds. As the reaction proceeds, the secondary nucleations will be likely to grow along with the surface of the $NiCo_2S_4$ initial nuclei rather than scattering in the solution.[13] At the same time, along with an Ostwald ripening process, the small $NiCo_2S_4$ nanoparticles gradually dissolve and gather again around some agglomerates, and thus larger structures are formed, which is driven by the minimization of surface energy.[27,28] As the reaction continues, the bigger nanoparticles further aggregate to form sphere-like superstructures and these superstructures prefer to cluster in groups. After further prolonged reaction time, 3D well-rounded cauliflower-like hierarchical microstructures are formed.

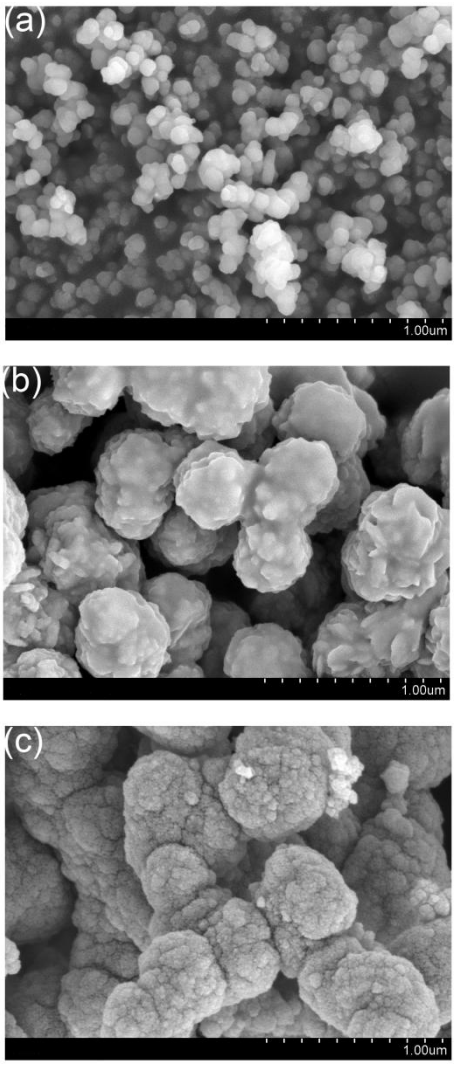

Fig. 4 SEM images of the materials obtained at different reaction stages: (a) 1.5 min, (b) 3 min, (c) 5 min.

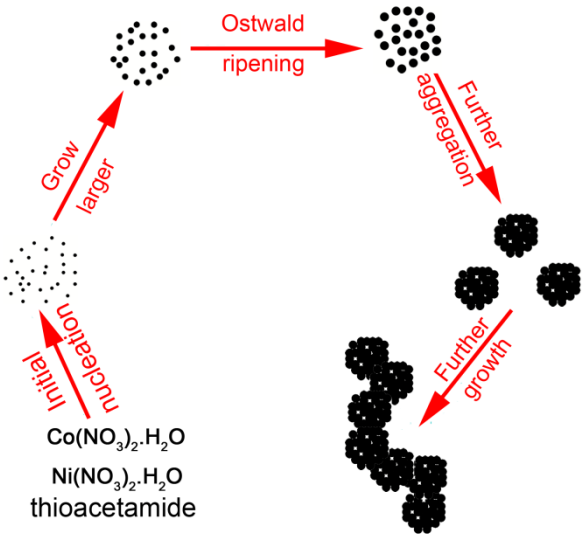

Fig. 5 Schematic illustration of possible growth process of the 3D cauliflower-like $NiCo_2S_4$ architectures.

Electrochemical property of the $NiCo_2S_4$ materials

To explore the performance of the $NiCo_2S_4$ in supercapacitors, the electrochemical property is tested by the CV method. Through electrochemical measurement, we optimized the experimental conditions, such as reaction time, reaction power, and with citric acid or not (Fig. S2, Fig. S3 and Fig. S4, ESI). The $NiCo_2S_4$ materials prepared at the optimal experimental conditions displays prominent electrochemical performance. Fig. 6a presents typical CV curves of the $NiCo_2S_4$ electrode with various scan rates (2, 5, 10, 20 and 30 mV s^{-1}) in the voltage range from -0.1 to 0.6 V. Apparently, the distinct redox peaks in each CV curve reveal that the pseudo-capacitive characteristics of the $NiCo_2S_4$ samples. The redox peaks may mostly result from the faradaic redox reactions related to $Co^{2+}/Co^{3+}/Co^{4+}$ and Ni^{2+}/Ni^{3+} redox couples. The faradaic reactions are proposed as follows:[18,19]

$$CoS + OH^- \leftrightarrow CoSOH + e^-$$
$$CoSOH + OH^- \leftrightarrow CoSO + H_2O + e^-$$
$$NiS + OH^- \leftrightarrow NiSOH + e^-$$

Because the redox potentials of Co^{2+}/Co^{3+} and Ni^{2+}/Ni^{3+} are near, the two redox peaks overlap together.[26] The first pair of redox peaks might be assigned to the redox reaction among from $NiCo_2S_4$ to NiSOH and CoSOH. Another pair probably come from the conversion between CoSOH and CoSO.[29] Moreover, the acetylene black added in the electrode can broad some redox peaks. Then the three pairs of redox peaks are not obvious.[26] The symmetrical CV curves indicate the good kinetic reversibility of $NiCo_2S_4$. As the scan rates increased, the current densities of the CV curves gradually increase and the oxidation and reduction peaks shift to more positive and negative potential, respectively. This may be attributed to the diffusion of OH^- ions. The OH^- ions diffuse more slowly at low scan rates, then the active materials can react fully with OH^- ions and have a higher utilization ratio.[18] As shown in the inset of Fig. 6a, good linear dependence of the current densities of anodic and cathodic peaks on the square root of the scan rates is shown, suggesting that the diffusion of OH^- is indeed the rate controlling process.[30]

Further evaluate the capacitive properties of $NiCo_2S_4$ sample, the charge-discharge measurements were performed at a voltage range from 0 to 0.5 V with various current densities (vs. Hg/HgO). As depicted in Fig. 6b and c, the shapes of galvanostatic charge-discharge curves show a representative pseudo-capacitive behaviour coming from the faradaic redox reactions, which is consistent with the CV results.[25] From the Fig. 6b and c, no obvious *iR* drops are observed at low current densities, indicating the good conductivity of the $NiCo_2S_4$.[17] The specific capacitances are calculated from the galvanostatic charge-discharge curves employing the following equation:[31]

$$C = \frac{I\Delta t}{\Delta V m}$$

where C, m, Δt, ΔV and I represent the specific capacitance, the weight of electroactive materials in the electrode, discharge time, potential change during discharge process, and charge or discharge current, respectively. Using the equation, the specific capacitances were estimated to be 1471, 1463, 1432, 1407, 1372, 1311, 1205, 1106 and 940 F g^{-1}, corresponding to the current densities of 1, 3, 5, 7, 10, 15, 25, 35 and 50 A g^{-1}, respectively, as shown in Fig. 6d. Compared with some Ni-Co compounds and the corresponding binary sulphides, CoS and NiS electrode materials,[11,13,17,18,19,32-35] the specific capacitances obtained in this work are prominent (see Table S2, ESI). Besides, the capacitance value at a much larger current density of 20 A g^{-1} is around 86.5% of that at 1 A g^{-1}. What's more, when the current density is increased 50-times from 1 to 50 A g^{-1}, the specific capacitance still retains 63.9%, which is prominent compared to those of Ni-Co compounds electrode materials (Table S2). These results suggest that the as-prepared 3D $NiCo_2S_4$ materials deliver remarkably high capacitance value and enhanced capacitance retention. The high electrochemical characteristics of the $NiCo_2S_4$ materials are probably attributed to the activation process for the 3D cauliflower-like $NiCo_2S_4$ electrode (Fig. S5, ESI).[36,37] After activation, the surface of the $NiCo_2S_4$ electrode may produce more electroactive sites, which may contribute to the increase of specific capacitance.[38] In addition, there are some mesoporous and microporous structures in the $NiCo_2S_4$ material (Fig. S6, ESI). The mesoporous structure plays an important role in the electrochemical measurement, which can promote the diffusion of the electrolyte ions inside the electroactive materials.[30] It is worth pointing out that the microporous structures also could play an important role in the activated process. Specifically, these microporous structure may also contribute to the diffusion of electrolytes into the materials and also be used for charge accommodation, which makes contribution to the specific capacitance increase.[39]

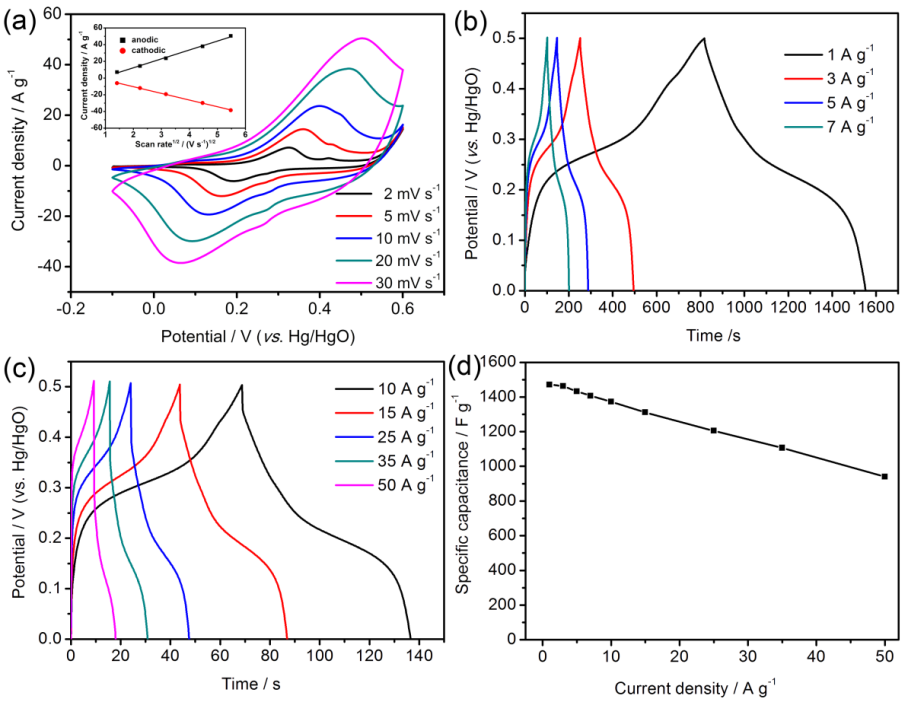

Fig. 6 (a) CV curves with various scan rates (Inset: the plots of the current densities of anodic and cathodic peaks versus the square root of the scan rate) and (b and c) galvanostatic charge-discharge curves at various current densities of the $NiCo_2S_4$-modified electrode in 6 M KOH solution. (d) The corresponding capacitance values versus current densities.

The stability of the $NiCo_2S_4$ sample is also important for supercapacitors. Consecutive galvanostatic charge-discharge was investigated at 10 A g^{-1} between 0 and 0.5 V for 1000 repetitive cycles, the corresponding result is shown in Fig. 7a. For the $NiCo_2S_4$ electrode, the specific capacitance hardly changes in the first 500 cycles. As the cycle numbers continue to increasing, the specific capacitance gradually decreases. After 1000 cycles, the specific capacitance can still retain 94.9% of the initial value, indicating its remarkable cycling stability. What's more, during the entire cycling test, the coulombic efficiency (η) almost remains unchanged at ~100%, suggesting the redox process within the $NiCo_2S_4$ materials is highly reversible. These results

reveal that the as-obtained 3D cauliflower-like $NiCo_2S_4$ have excellent performance in pseudocapacitors.

Further understand electrochemical properties of the $NiCo_2S_4$-modified electrode, the EIS measurements were carried out before and after the cycle tests and the corresponding Nyquist plots are displayed in Fig. 7b. The EIS spectra are composed of a sloped line at the low-frequency and one small arc at the high-frequency. The enlarge view of the high-frequency and the equivalent circuit according to the EIS are shown in the insets of Fig. 7b, where R_s composed of the inherent resistance of electrode materials, electrolyte resistance, and contact resistance at the interface between materials and current collector,[40] is a bulk solution resistance. R_{ct} is the charge-transfer resistance, CPE and C_F respectively represent a double-layer capacitor, a faradaic pseudocapacitance. The Warburg impedance is attributed to the diffusive resistance of the electrolyte ion within the $NiCo_2S_4$ modified electrodes.[40] R_s and R_{ct} are characterized by the high-frequency intercept on the real axis at R_s and (R_s + R_{ct}), respectively. Before and after the cycling tests, the resistances of the bulk solution (R_s) are 0.491 and 0.518 Ω, respectively. And the values of R_{ct} are 0.290 and 0.301 Ω, respectively. The results are in good accordance with the slight decrease of the specific capacitance after the cycle test and reveal that the 3D cauliflower-like $NiCo_2S_4$ architectures have excellent electrochemical performance.

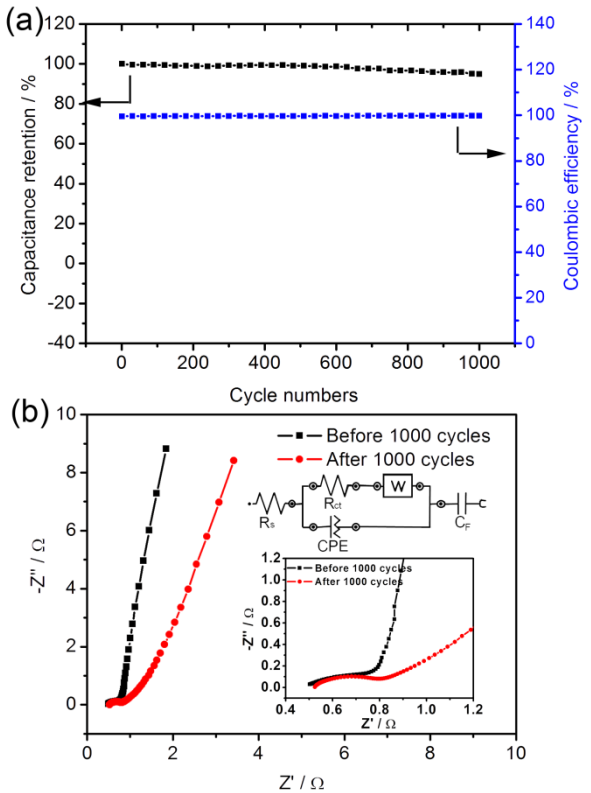

Fig. 7 (a) Cycle performance and coulombic efficiency of the $NiCo_2S_4$-modified electrode at 10 A g^{-1} in 6 M KOH. (b) EIS plots of the $NiCo_2S_4$ materials before and after 1000 cycle charge-discharge test. The inset displays an enlarge view and the equivalent circuit based on EIS.

Electrochemical performance of the $NiCo_2S_4$//AC asymmetric capacitors

To further investigate the practical application of the $NiCo_2S_4$ material, an asymmetric capacitor was fabricated employing the $NiCo_2S_4$-modified electrode as the positive electrode and the activated carbon-modified electrode (the electrochemical performance details in Fig. S8, ESI) as the negative electrode. The typical weight ratio between the positive and negative is calculated based on the following equation:[37]

$$\frac{m_+}{m_-} = \frac{C_- \times \Delta E_-}{C_+ \times \Delta E_+}$$

where ΔE_+ and ΔE_- are the potential range for positive and negative electrodes, respectively. C_+ and C_- are the specific capacitance measured in the same condition for positive and negative electrodes, respectively. m_+ and m_- represent the weight of electroactive materials for positive and negative electrodes, respectively. Based on the equation above, the weight ratio between AC and $NiCo_2S_4$ is calculated to be 3.03. Fig. 8a presents the CV curves of the $NiCo_2S_4$//AC asymmetric capacitor with various scan rates. The voltage window of the asymmetric supercapacitor can be extend up to 1.6 V, according to the electrochemical performance of $NiCo_2S_4$ and AC electrodes measured in a three- electrode system (Fig. S9, ESI). These CV curves show electric double layer capacitive and pseudo-capacitive properties between AC and $NiCo_2S_4$, respectively. Fig. 8b and c show the galvanostatic charge-discharge curves of the asymmetric capacitor with different current densities and the results are shown in Fig. 8d. Obviously, the asymmetric supercapacitor presents the maximum capacitance value of 126 F g^{-1} at 0.5 A g^{-1}. Moreover, the specific capacitance at 20 A g^{-1} is still around 52% of that at 0.5 A g^{-1}, indicating remarkable rate capability.

Based on the galvanostatic charge-discharge measurements, the energy density and power density of the asymmetric supercapacitor were estimated based on the following equations:[40]

$$E = \frac{1}{2} C \Delta V^2$$

$$P = \frac{E}{\Delta t}$$

where E, P, C, Δt, and ΔV are the energy density, power density, specific capacitance, discharge time, and potential change during discharge process, respectively. Fig. 8e presents the Ragone plot of asymmetric supercapacitor. Remarkably, the asymmetric capacitor presents the maximum energy density of 44.8 Wh kg^{-1} at 0.5 A g^{-1}, and the corresponding power density is 401 W kg^{-1}. After 40-time increase in the current density, the power density can reach 16.0 kW kg^{-1}, while the energy density can still retain 23.1 Wh kg^{-1}, which displays their superiority as a potential candidate for supercapacitor. The large capacitance value and large potential window make great contributions to the high energy density. Obviously, our $NiCo_2S_4$//AC supercapacitor presents remarkable performance compared to other Ni-Co compounds assembled asymmetric capacitors, such as Ni-Co sulfide nanowires on Ni foam//AC (25.0 Wh kg^{-1}),[42] $NiCo_2S_4$ nanotube arrays on Ni foam//RGO (31.5 Wh kg^{-1}),[43] Ni_xCo_{1-x}LDH-ZTO heterostructure//AC (23.7 Wh kg^{-1}),[44] porous CQDs/$NiCo_2O_4$ composite//AC (27.8 Wh kg^{-1}),[45] and $NiCo_2O_4$-RGO composite//AC (23.3 Wh kg^{-1}).[46]

The cycle performance and coulombic efficiency of the $NiCo_2S_4$//AC-based asymmetric capacitor were carried out at 6 A g^{-1} for 3000 cycles. As depicted in Fig. 8f, the asymmetric supercapacitor shows remarkable cycle stability with only 5% decrease of the initial value after 3000 cycles. The prominent cycling characteristics of the asymmetric capacitor might be ascribed to the incorporation of activated carbon (AC). In the three-electrode system, both the $NiCo_2S_4$-modified electrode and AC-modified electrode exhibit prominent cycling characteristics (Fig. 7a and Fig. S8d). So in the two-electrode system, the synergy of the two electrodes makes the $NiCo_2S_4$//AC-based asymmetric capacitor show better cycle stability, and the similar phenomenon was also performed in previous reports.[47,48] Furthermore, the asymmetric supercapacitor exhibits a high coulombic efficiency of ~99%. These results demonstrate the outstanding electrochemical performance of the $NiCo_2S_4$//AC asymmetric supercapacitor. What's more, two assembled asymmetric capacitors can light up a 5 mm-diameter red (2.0 V, 20 mA) round light-emitting diode (LED) and last for more than 10 min (Fig. 8g and h). It clearly indicates that the assembled $NiCo_2S_4$//AC asymmetric capacitor has remarkable electrochemical characteristics and the $NiCo_2S_4$ materials have a great potential in practical application of supercapacitors.

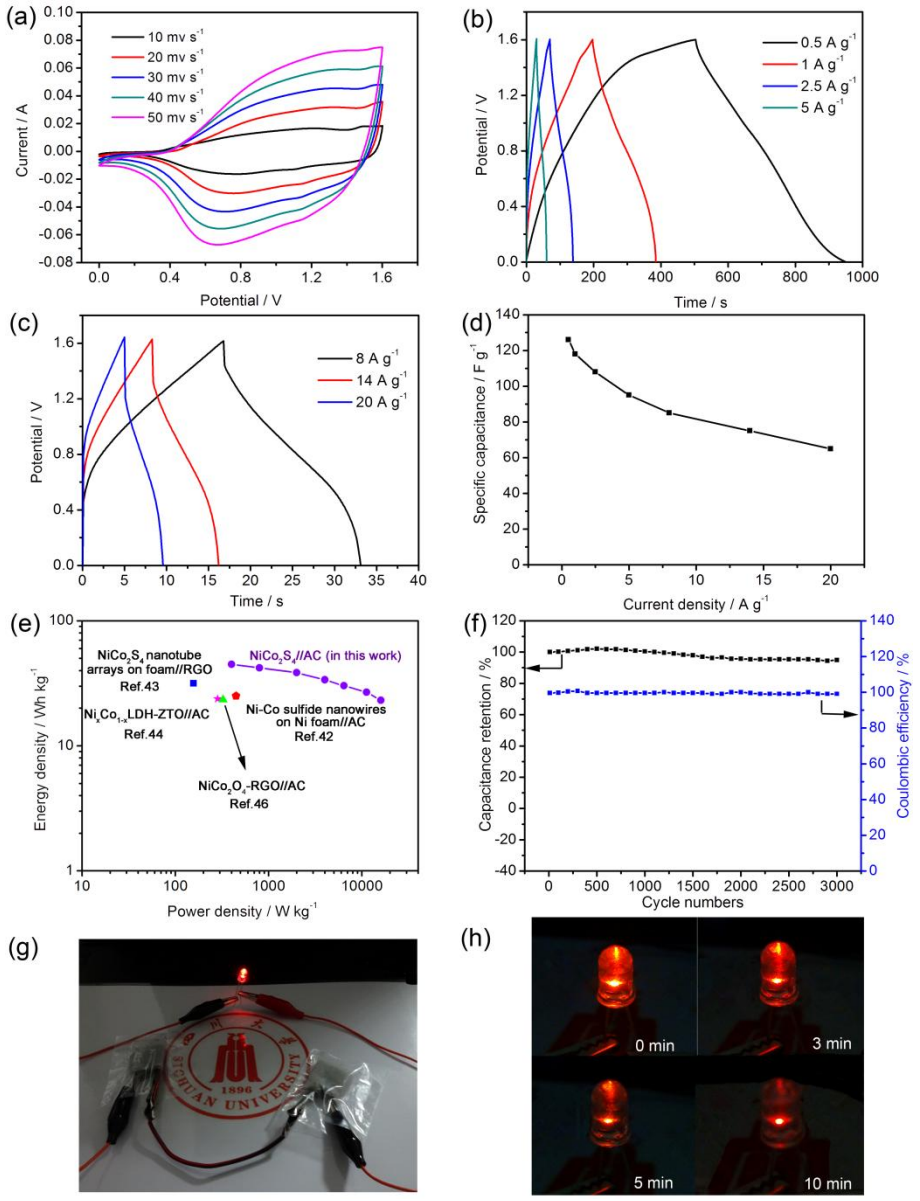

Fig. 8 (a) CV curves at different scan rates and (b and c) charge-discharge curves at various current densities of the $NiCo_2S_4$//AC-based asymmetric capacitor in 6 M KOH solution. (d) The corresponding specific capacitances. (e) Ragone plots and (f) the cycle performance and coulombic efficiency of the asymmetric capacitor at 6 A g^{-1}. (g) A photograph presenting two $NiCo_2S_4$//AC-based asymmetric capacitors assembled together can power a red LED. (h) Photographs of the red LED at various time of duration.

Conclusions

In conclusion, 3D cauliflower-like $NiCo_2S_4$ architectures were successfully fabricated by a facile, rapid MWH method. The $NiCo_2S_4$ samples exhibit high specific capacitance (1471 F g^{-1} at 1 A g^{-1}), as well as remarkable rate capability and cycling characteristics (94.9% retention after 1000 cycles). The as-fabricated asymmetric supercapacitor exhibits the highest energy density of 44.8 Wh kg^{-1} and the highest power density of 16 kW kg^{-1}. In addition, the asymmetric supercapacitor also presents prominent cycle performance with ~95% retained after 3000 charging-discharging cycles. The prominent capacitance performance of the 3D cauliflower-like $NiCo_2S_4$ indicate that it is a potential material for supercapacitor.

Acknowledgements

This work was financially supported by the National Natural Science Foundation of China (Nos. 21177090, 21275104) and the China Postdoctoral Science Foundation (2013M531962).

Notes and references

[a]*College of Chemistry and* [b]*College of Chemical Engineering, Sichuan University, 29 Wangjiang Road, Chengdu 610064, China.*
**Corresponding author Tel: +86-28-85416029. Fax: +86-28-85415029. E-mail: xiaodan@scu.edu.cn.*

†Electronic Supplementary Information (ESI) available: Preparation of Activated Carbon (AC), the relative content of Co^{2+} and Co^{3+} as well as Ni^{2+} and Ni^{3+} in $NiCo_2S_4$, XRD patterns of the samples collected at different time, the electrochemical performance of the samples collected at different time, different reaction power and with citric acid or not, cycling ability of $NiCo_2S_4$, BET of $NiCo_2S_4$, BET of AC, the electrochemical performance of AC, the CV of $NiCo_2S_4$ and AC, a table including specific capacitance and capacitance retention of electroactive materials. See DOI: 10.1039/c0××00000×.

1. N. S. Lewis and D. G. Nocera, *Pro. Natl. Acad. Sci. U. S. A.*, 2006, **103,** 15729-15735.
2. C. Liu, F. Li, L. P. Ma and H. M. Cheng, *Adv. Mater.*, 2010, **22,** E28-E62.
3. H. Jiang, T. Zhao, J. Ma, C. Y. Yan and C. Z. Li, *Chem. Commun.*, 2011, **47,** 1264-1266.
4. H. Jiang, J. Ma and C. Z. Li, *Adv. Mater.*, 2012, **24,** 4197-4202.
5. L. Li, Y. Q. Zhang, F. Shi, Y. J. Zhang, J. H. Zhang, C. D. Gu, X. L. Wang and J. P. Tu, *ACS Appl. Mater. Interfaces*, 2014, **6,** 18040-18047.
6. W. Wang, S. R. Guo, M. Penchev, I. Ruiz, K. N. Bozhilov, D. Yan, M. Ozkan and C. S. Ozkan, *Nano Energy*, 2013, **2,** 294-303.
7. G. A. Snook, P. Kao and A. S. Best, *J. Power Sources*, 2011, **196,** 1-12.
8. S. K. Meher, P. Justin and G. R. Rao, *Nanoscale*, 2011, **3,** 683-692.
9. X. Wang, C. Y. Yan, A. Sumboja and P. S. Lee, *Nano Energy*, 2014, **3,** 119-126.
10. Y. F. Zhang, M. Z. Ma, J. Yang, H. Q. Su, W. Huang and X. C. Dong, *Nanoscale*, 2014, **6,** 4303-4308.
11. H. L. Wang, Q. M. Gao and L. Jiang, *Small*, 2011, **7,** 2454-2459.
12. J. W. Xiao, L. Wan, S. H. Yang, F. Xiao and S. Wang, *Nano lett.*, 2014, **14,** 831-838.
13. S. J. Peng, L. L. Li, C. C. Li, H. T. Tan, R. Cai, H. Yu, S. Mhaisalkar, M. Srinivasan, S. Ramakrishna and Q. Y. Yan, *Chem. Commun.*, 2013, **49,** 10178-10180.
14. Z. Y. Zhang, X. G. Wang, G. L. Cui, A. H. Zhang, X. H. Zhou, H. X. Xu and L. Gu, *Nanoscale*, 2014, **6,** 3540-3544.
15. Y. Liu, J. N. Zhang, S. P. Wang, K. X. Wang, Z. M. Chen and Q. Xu, *New J. Chem.*, 2014, **38**, 4045-4048.
16. J. F. Li, S. L. Xiong, Y. R. Liu, Z. C. Ju and Y. T. Qian, *ACS Appl. Mater. Interfaces*, 2013, **5,** 981-988.
17. H. C. Chen, J. J. Jiang, L. Zhang, H. Z. Wan, T. Qi and D. D. Xia, *Nanoscale*, 2013, **5,** 8879-8883.
18. J. Pu, T. T. Wang, H. Y. Wang, Y. Tong, C. C. Lu, W. Kong and Z. H. Wang, *ChemPlusChem*, 2014, **79,** 577-583.
19. H. Z. Wan, J. J. Jiang, J. W. Yu, K. Xu, L. Miao, L. Zhang, H. C. Chen and Y. J. Ruan, *CrystEngComm*, 2013, **15,** 7649-7651.
20. W. Chen, C. Xia and H. N. Alshareef, *ACS Nano*, 2014, **8**, 9531-9541.
21. Z. H. Ai, K. J. Deng, Q. F. Wan, L. Z. Zhang and S. C. Lee, *J. Phys. Chem. C*, 2010, **114,** 6237-6242.
22. S. K. Meher, P. Justin and G. Ranga Rao, *ACS Appl. Mater. Interfaces*, 2011, **3,** 2063-2073.
23. J. W. Xiao, X. W. Zeng, W. Chen, F. Xiao and S. Wang, *Chem. Commun.*, 2013, **49,** 11734-11736.
24. C. Z. Yuan, J. Y. Li, L. Hou, L. R. Yang, L. F. Shen and X. G. Zhang, *J. Mater. Chem.*, 2012, **22,** 16084-16090.
25. J. F. Marco, J. R. Gancedo, M. Gracia, J. L. Gautier, E. I. R ós, H. M. Palmer, C. Greaves and F. J. Berry, *J. Mater. Chem.*, 2001, **11,** 3087-3093.
26. Y. Lei, J. Li, Y. Y. Wang, L. Gu, Y. F. Chang, H. Y. Yuan and D. Xiao, *ACS Appl. Mater. Interfaces*, 2014, **6**, 1773-1780.
27. F. L. Luo, J. Li, H. Y. Yuan and D. Xiao, *Electrochimi. Acta*, 2014, **123,** 183-189.
28. L. S. Zhang, W. Z. Wang, Z. G. Chen, L. Zhou, H. L. Xu and W. Zhu, *J. Mater. Chem.*, 2007, **17,** 2526-2532.
29. L. F. Shen, J. Wang, G. Y. Xu, H. S. Li, H. Dou and X. G. Zhang, *Adv. Energy Mater.*,2014, **5**, 1400977.
30. J. Li, F. L. Luo, Q. Zhao, Z. P. Li, H. Y. Yuan and D. Xiao, *J. Mater. Chem. A*, 2014, **2,** 4690-4697.
31. D. P. Dubal, V. J. Fulari and C. D. Lokhande, *Micropor. Mesopor. Mater.*, 2012, **151,** 511-516.
32. W. M. Du, Z. Q. Zhu, Y. B. Wang, J. N. Liu, W. J. Yang, X. F. Qian and H. Pang, *RSC Adv.*, 2014, **4,** 6998-7002.
33. L. Yu, H. B. Wu, T. Wu and C. Z. Yuan, *RSC Adv.*, 2013, **3,** 23709-23714.
34. T. Zhu, Z. Y. Wang, S. J. Ding, J. S. Chen and X. W. D. Lou, *RSC Adv.*, 2011, **1,** 397-400.
35. L. Zhang, H. B. Wu and X. W. Lou, *Chem. Commun.*, 2012, **48,** 6912-6914.
36. H. Jiang, J. Ma and C. Z. Li, *Chem. Commun.*, 2012, **48,** 4465-4467.
37. G. X. Hu, C. H. Tang, C. X. Li, H. M. Li, Y. Wang and H. Gong, *J. Electrochem. Soc.*, 2011, **158,** A695-A699.
38. H. C. Chen, J. J. Jiang, Y. D. Zhao, L. Zhang, D. Q. Guo and D. D. Xia, *J. Mater. Chem. A*, 2015, **3,** 428-437.
39. D. W. Wang, F. Li, M. Liu, G. Q. Lu and H. M. Cheng, *Angew. Chem.*, 2008, **120,** 379-382.
40. Y. Y. Wang, Y. Lei, J. Li, L. Gu, H. Y. Yuan and D. Xiao, *ACS Appl. Mater. Interfaces*, 2014, **6,** 6739-6747.
41. V. Khomenko, E. Raymundo-Pinero and F. B éguin, *J. Power Sources*, 2006, **153,** 183-190.
42. Y. H. Li, L. J. Cao, L. Qiao, M. Zhou, Y. Yang, P. Xiao and Y. H. Zhang, *J. Mater. Chem. A*, 2014, **2,** 6540-6548.
43. H. C. Chen, J. J. Jiang, L. Zhang, D. D. Xia, Y. D. Zhao, D. Q. Guo, T. Qi and H. Z. Wan, *J. Power Sources*, 2014, **254,** 249-257.
44. X. Wang, A. Sumboja, M. F. Lin, J. Yan and P. S. Lee, *Nanoscale*, 2012, **4,** 7266-7272.
45. Y. R. Zhu, Z. B. Wu, M. J. Jing, H. S. Hou, Y. C. Yang, Y. Zhang, X. M. Yang, W. X. Song, X. N. Jia and X. B. Ji, *J. Mater. Chem. A*, 2015, **3,** 866-877.
46. X. Wang, W. S. Liu, X. H. Lu and P. S. Lee, *J. Mater. Chem.*, 2012, **22,** 23114-23119.
47. M. J. Jing, Y. C. Yang, Y. R. Zhu, H. S. Hou, Z. B. Wu and X. B. Ji, *Electrochimi. Acta*, 2014, **141,** 234-240.
48. J. Yan, Z. J. Fan, W. Sun, G. Q. Ning, T. Wei, Q. Zhang, R. F. Zhang, L. J. Zhi and F. Wei, *Adv. Funct. Mater.*, 2012, **22,** 2632-2641.